Satellite to Ground Look Geometry
one pass

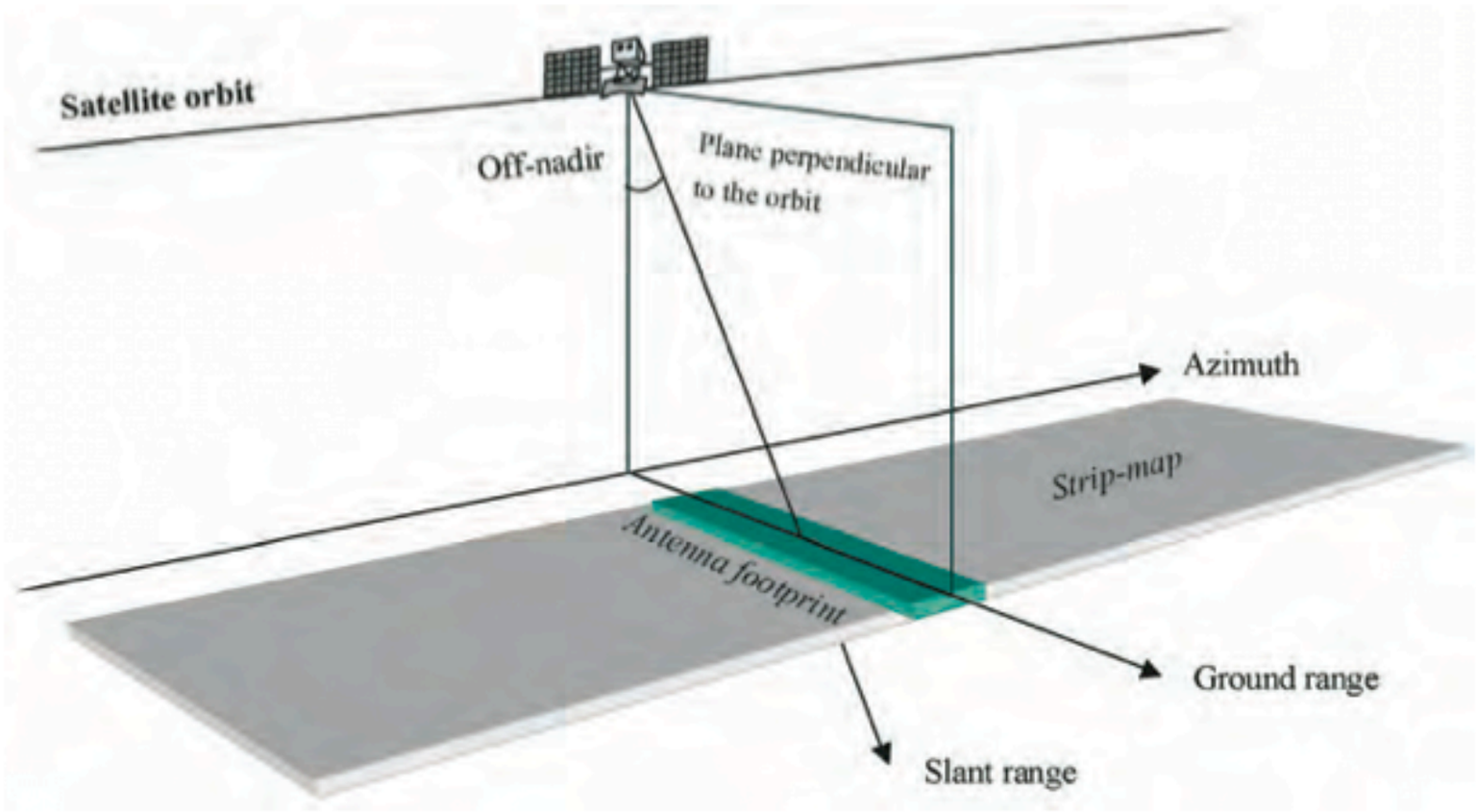

Figure 1-3: A SAR system from a satellite

Ferretti et al., 2007

Different Types of Satellite Interferometry for topography oceanography, deformation

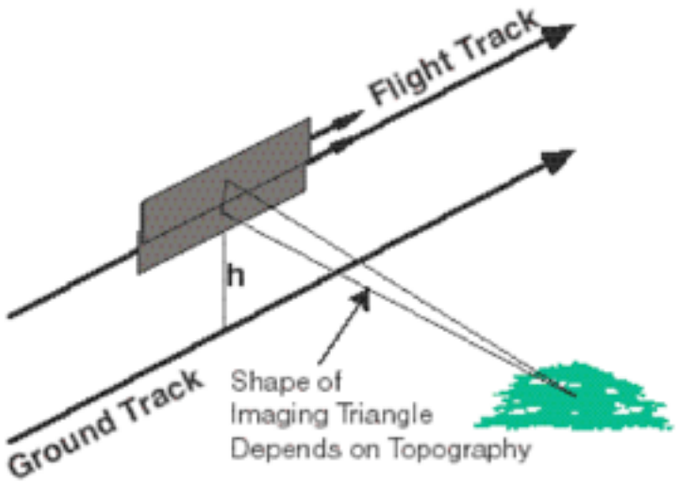

Figure 3: Interferometric SAR for topographic mapping uses two apertures separated by a "baseline" to image the surface. The phase difference between the apertures for each image point, along with the range and knowledge of the baseline, can be used to infer the precise shape of the imaging triangle to derive the topographic height of the image point.

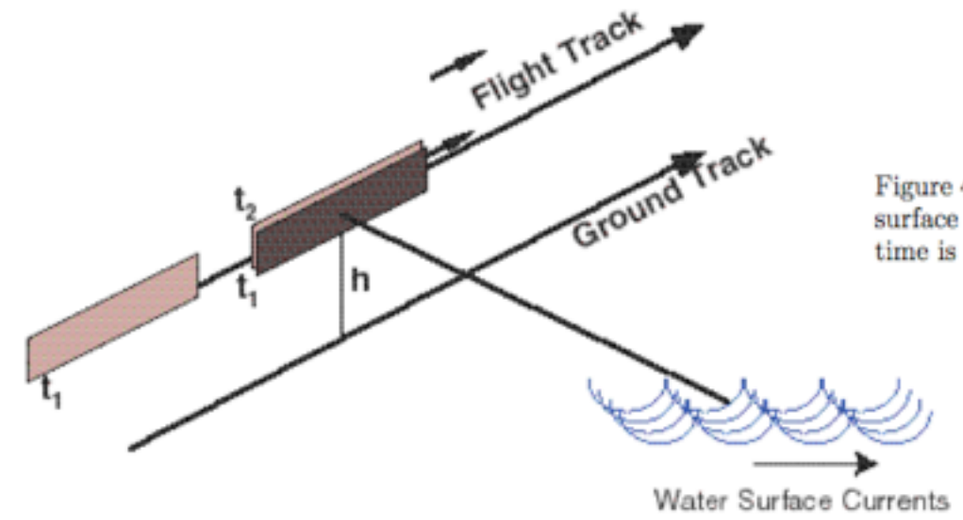

Figure 4: An along track interferometer maintains a baseline separated along the flight track such that surface points are imaged by each aperture within one second. Motion of the surface over the elapsed time is recorded in the phase difference of the pixels.

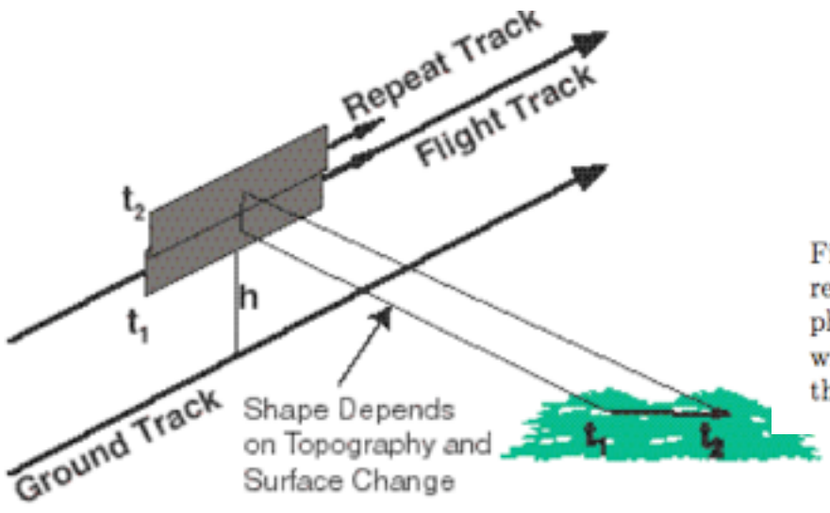

Figure 5: A repeat track interferometer is similar to an along track interferometer. An aperture repeats its track and precisely measures motion of the surface between observations in the image phase difference. If the track does not repeat at exactly the same location, some topographic phase will also be present, which must be removed by the methods of differential interferometry to isolate the motion.

Rosen et al., 2000

Radar Topography

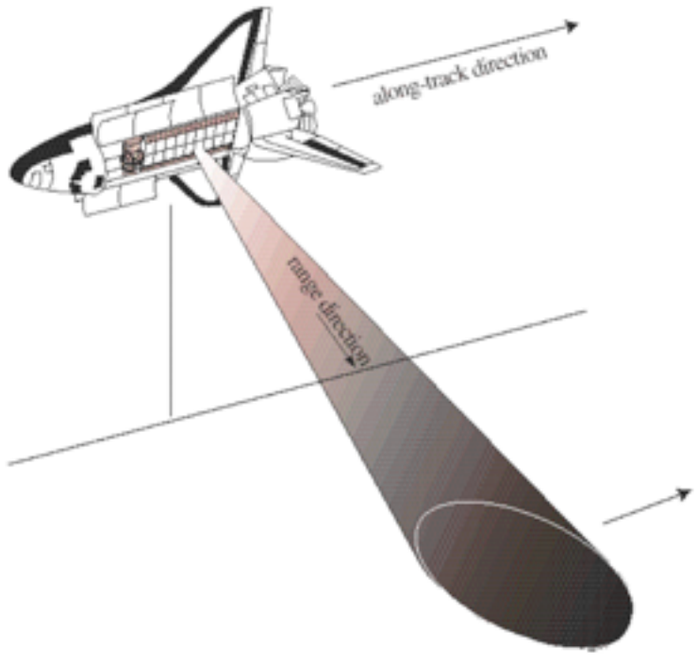

Figure 1: Typical imaging scenario for a SAR system, depicted here as a shuttle-borne radar. The platform carrying the SAR instrument follows a curvilinear track known as the "along-track," or "azimuth," direction. The radar antenna points to the side, imaging the terrain below. The distance from the aperture to a target on the surface in the look direction is known as the "range." The "cross-track," or range, direction is defined along by the range, and is terrain dependent.

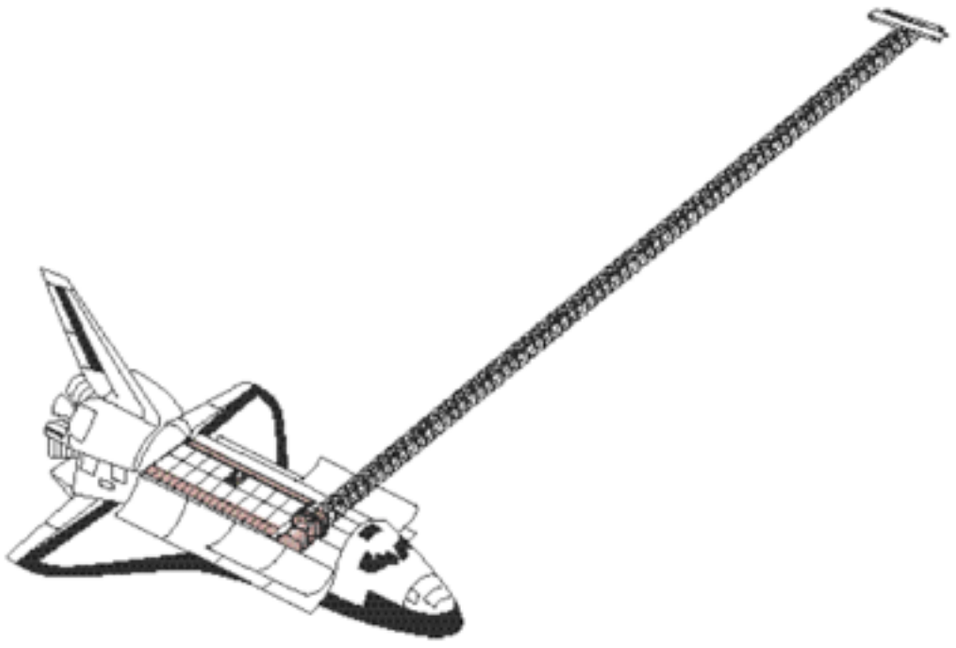

Figure 26: The Shuttle Radar Topography Mission flight system configuration. The SIR-C/X-SAR L, C, and X-band antennas reside in the shuttle's cargo bay. The C and X band radar systems are augmented by receive-only antennas deployed at the end of a 60 m long boom. Interferometric baseline length and attitude measurement devices are mounted on a plate attached to the main L-band antenna structure. During mapping operations, the shuttle is oriented to that the boom is 45 degrees from the horizontal.

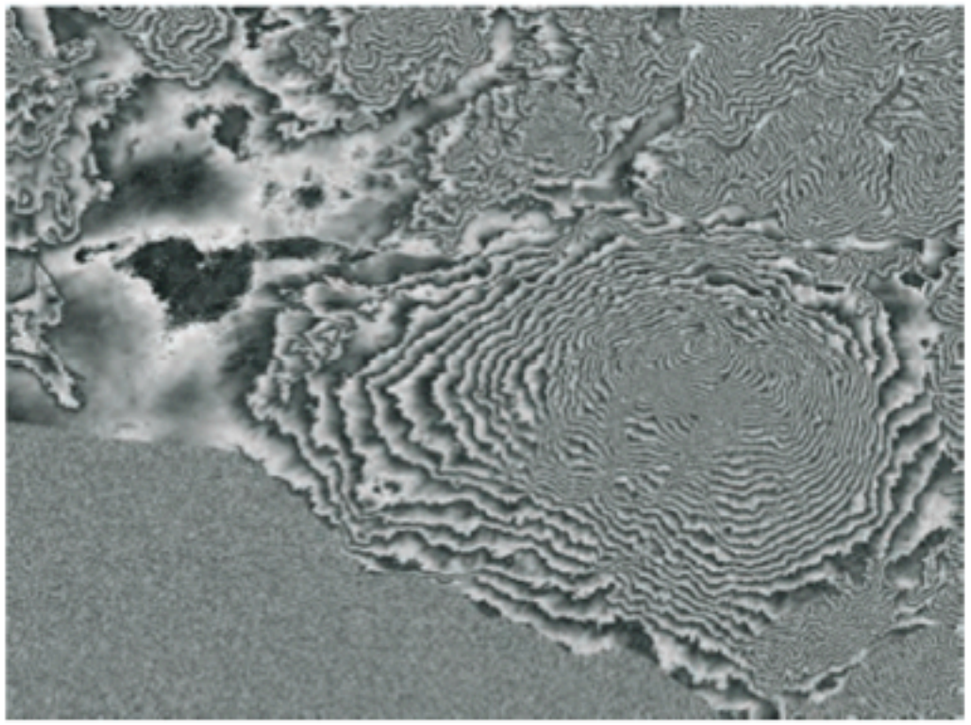

Figure 2-5: Flattened interferogram of Mount Etna generated from ERS tandem pairs. The perpendicular baseline of 115 metres generates an altitude of ambiguity of about 82 metres.

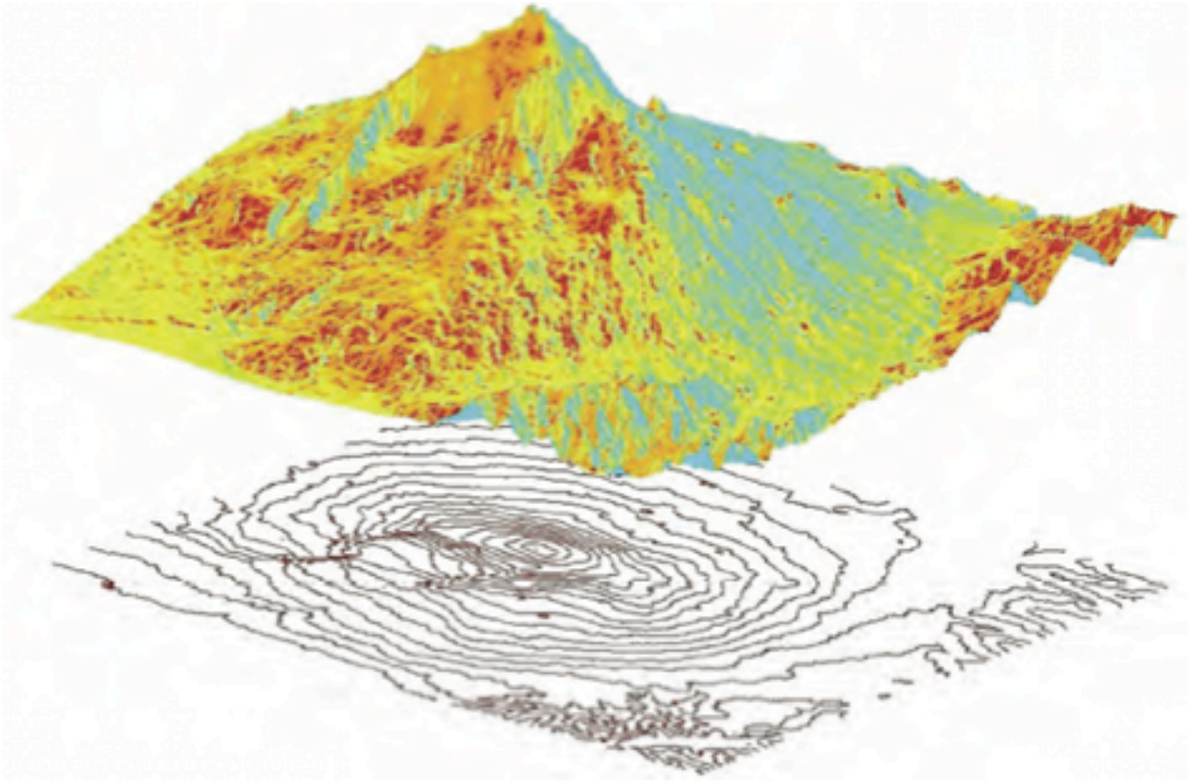

Figure 2-6: Perspective view of Mount Etna as seen from the Northeast. The DEM of Mount Etna has been generated by unwrapping and re-sampling the flattened interferogram of Figure 2-5: The estimated vertical accuracy is better than 10 metres. Contour lines are shown below the DEM.

A familiar place

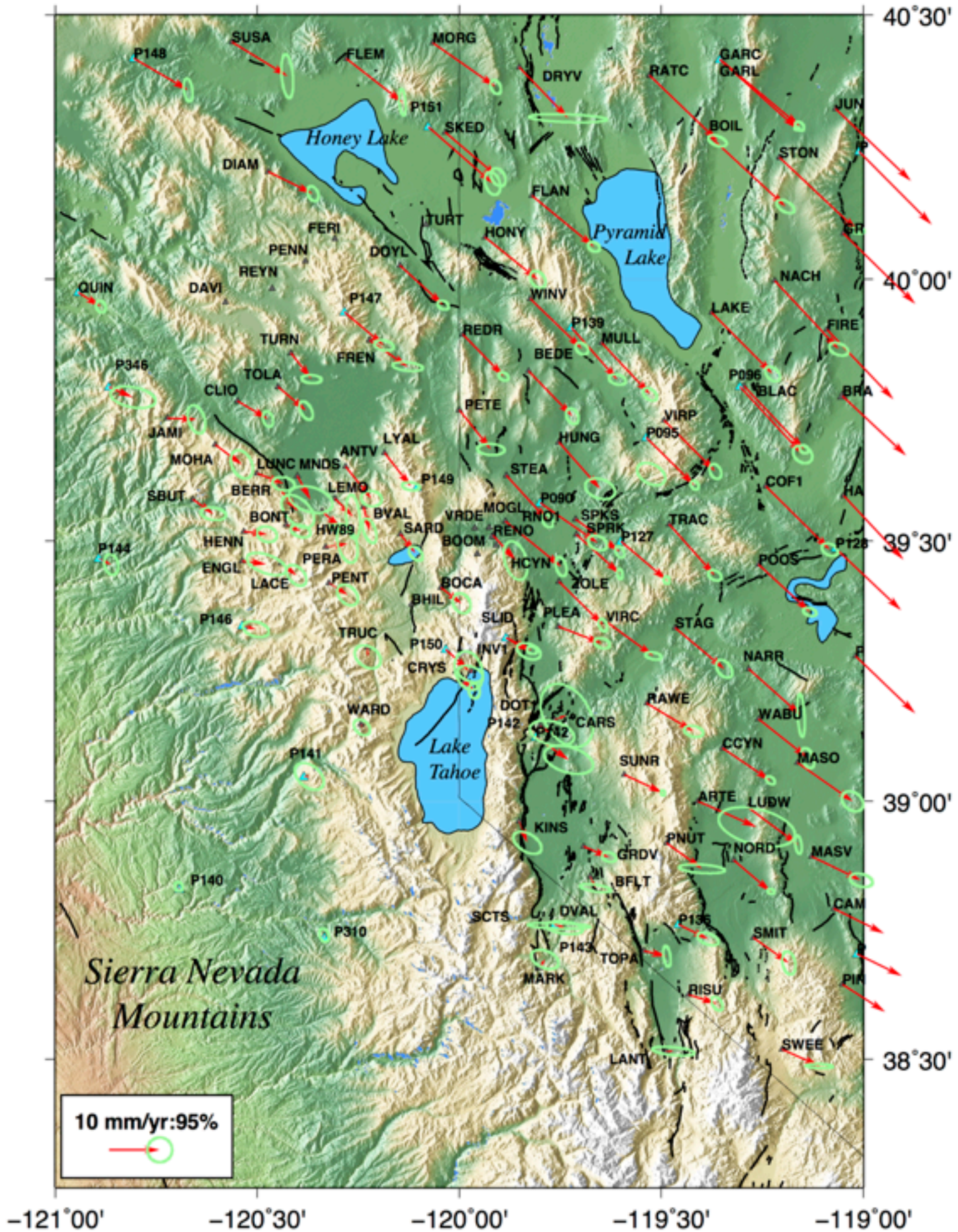

Satellite to Ground Look Geometry
two pass

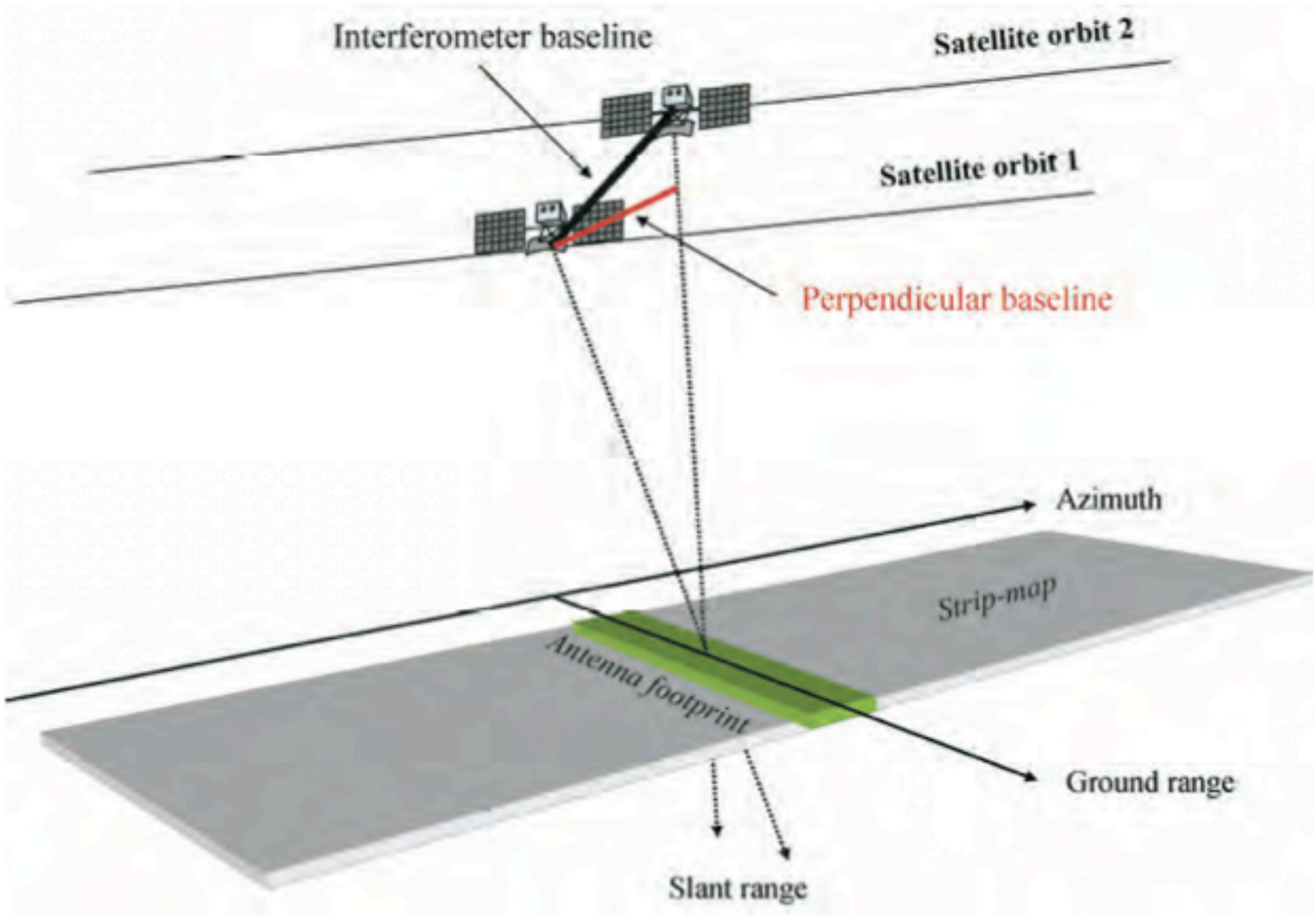

Figure 2-1: Geometry of a satellite interferometric SAR system. The orbit separation is called the interferometer baseline, and its projection perpendicular to the slant range direction is one of the key parameters of SAR interferometry.

Ferretti et al., 2007

Satellite Baseline and Surface Displacement Vectors

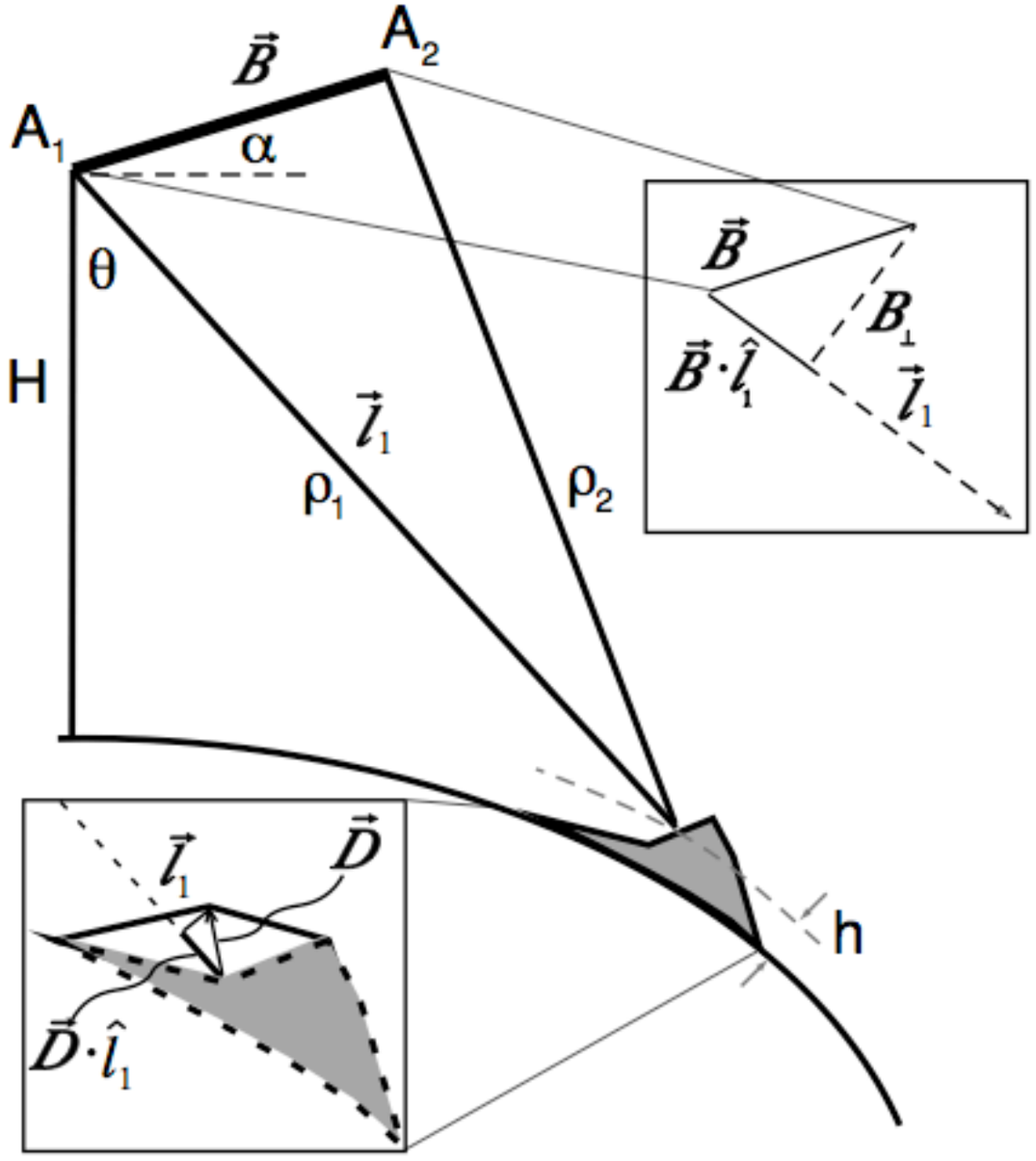

Figure 1 Imaging geometry of side-looking radar for InSAR applications. The *box* in the *top right* illustrates the contribution of the orbit separation baseline to measured range differences. The *box* in the *bottom left* illustrates the range change caused by the surface displacement component in the range direction. See text for discussion and explanation.

from Burgmann et al., 2000 and Rosen et al., 2000

1992 Fawnskin earthquake, ~M5
Mojave

Feigl & Thurber, 2009

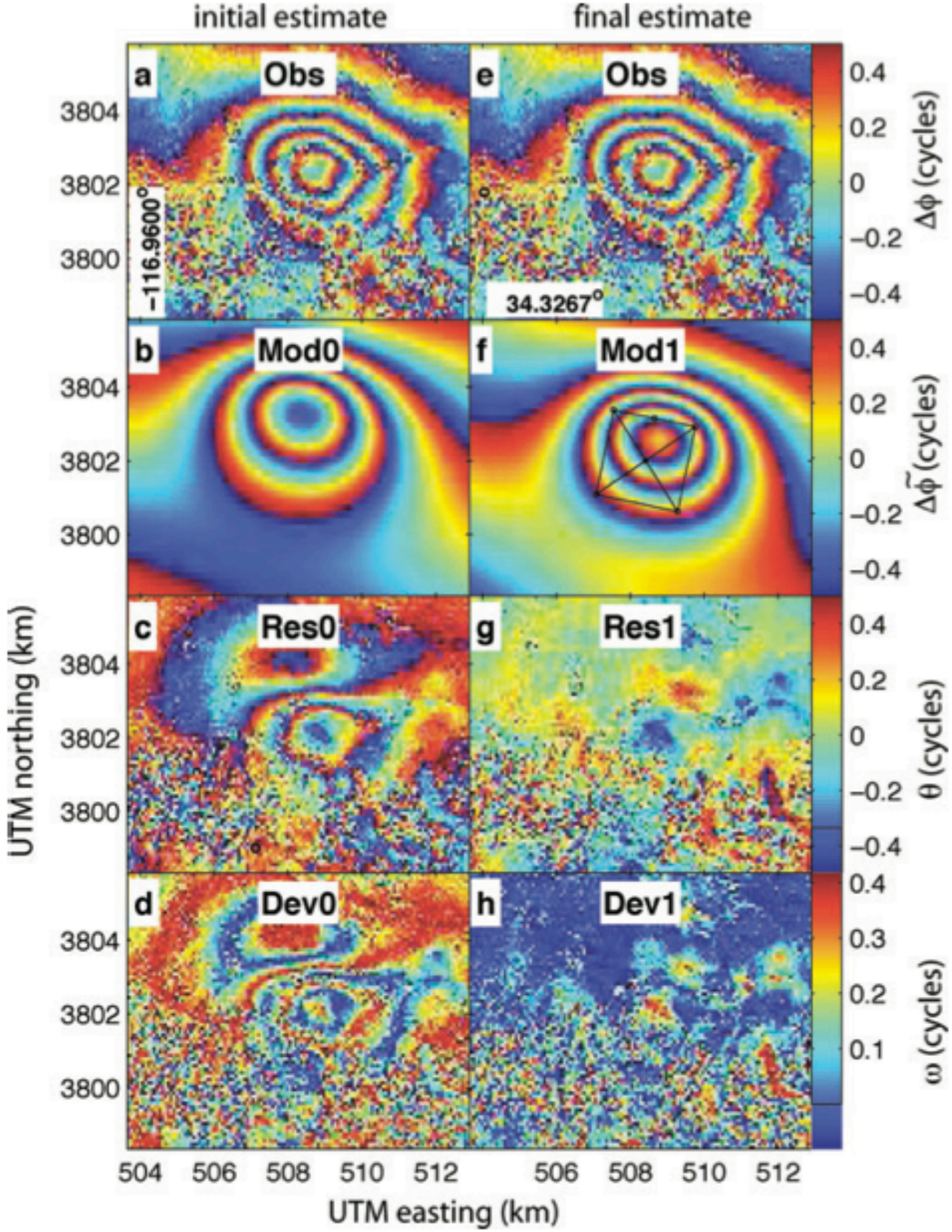

Problems when Topography is Steep
Layover and Shadow

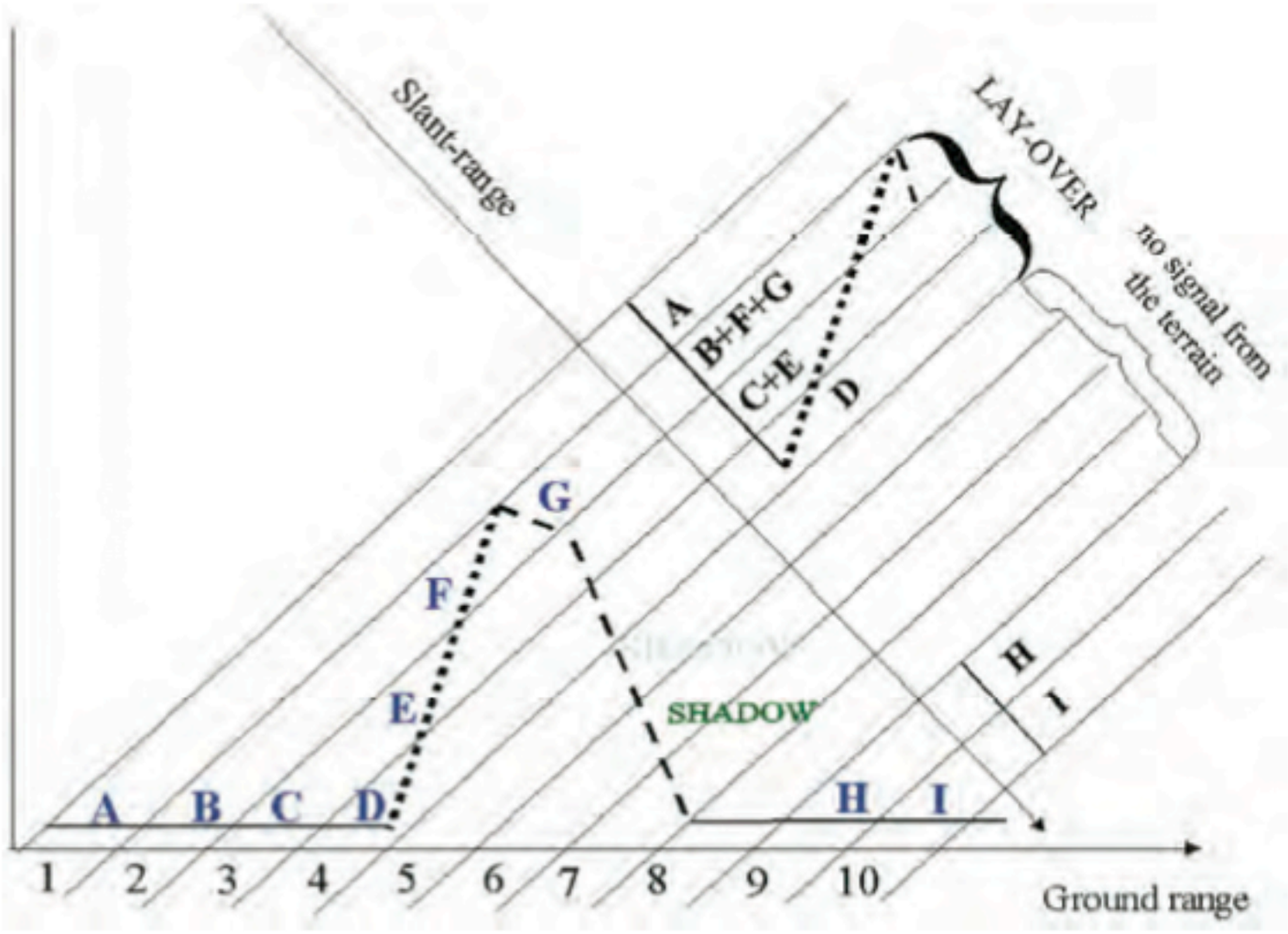

Figure 1-10: Layover and shadow effects. Depending on the terrain slope, scatterers that are located at increasing ground range positions can be imaged in reverse order by the SAR system (points D, E, F and G). Moreover they are imaged in the same SAR resolution cells as scatterers B and C, which belong to a different area on the ground (layover). On the other side of the elevation profile, scatterers located between points G and H cannot be illuminated by the radar since they are in shadow. As a consequence, SAR resolution cells from 5 to 8 do not contain any signal from the ground and they generate a dark gap on the detected image.

Estimating 3d displacement from multiple satellite look angles

[6] Suppose now that a point on the ground is observed in interferograms with four different look directions, for instance, with the antenna looking both right and left on both ascending and descending passes, or for two different incidence angles on ascending and descending passes. Defining $\mathbf{R} = (r_1, r_2, r_3, r_4)^T$, where r_i are the line-of-sight displacements for the different look directions, then $\mathbf{R} = -\mathbf{Pu}$ where $\mathbf{P}$ is the 4×3 matrix given by

$$\mathbf{P} = \begin{pmatrix} \hat{\mathbf{p}}_1 \\ \hat{\mathbf{p}}_2 \\ \hat{\mathbf{p}}_3 \\ \hat{\mathbf{p}}_4 \end{pmatrix} \tag{1}$$

If the covariance matrix for errors in the observed range changes is $\mathbf{\Sigma}_R$, then the weighted least-squares (maximum likelihood) solution for $\mathbf{u}$ is

$$\hat{\mathbf{u}} = -\left[\mathbf{P}^T \mathbf{\Sigma}_R^{-1} \mathbf{P}\right]^{-1} \mathbf{P}^T \mathbf{\Sigma}_R^{-1} \mathbf{R} \tag{2}$$

and the covariance matrix for the estimated vector components is

$$\mathbf{\Sigma}_u = \left[\mathbf{P}^T \mathbf{\Sigma}_R^{-1} \mathbf{P}\right]^{-1} \tag{3}$$

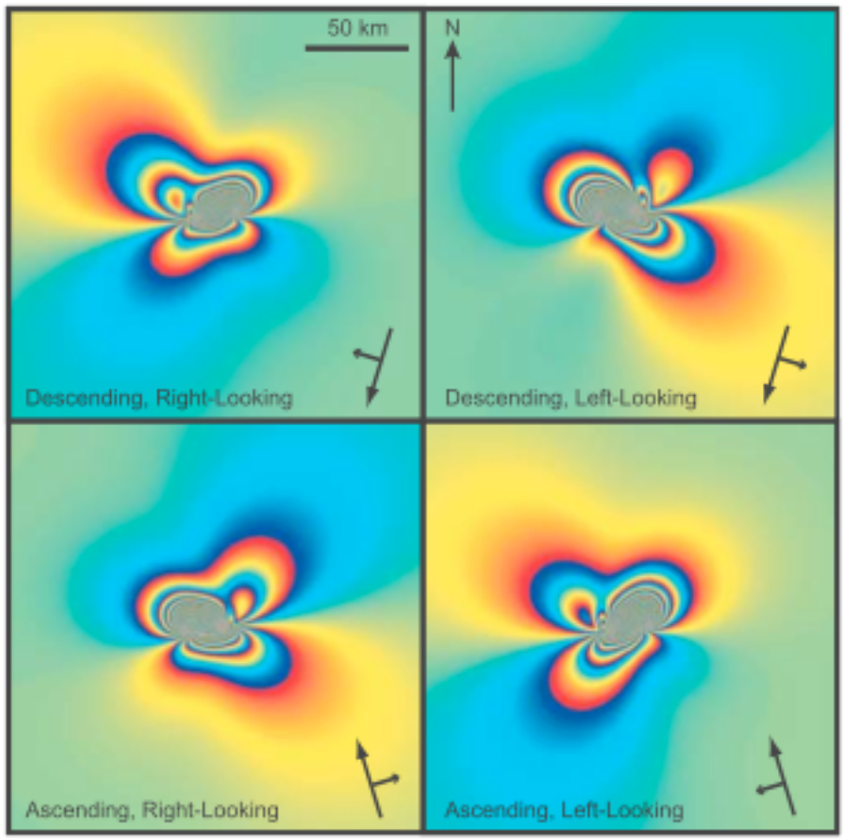

Figure 2. Synthetic interferograms for a Düzce-like earthquake [Strike/Dip/Rake/Depth Range/Length/Slip = 262°/52°/−175°/0–11 km/20 km/5 m], calculated with different viewing geometries (Case 2a; Table 1). Each fringe is equivalent to a range change of 100 mm, half of the wavelength of an L-band mission.

Wright et al., 2004, GRL

Estimating 3d displacement from multiple satellite look angles

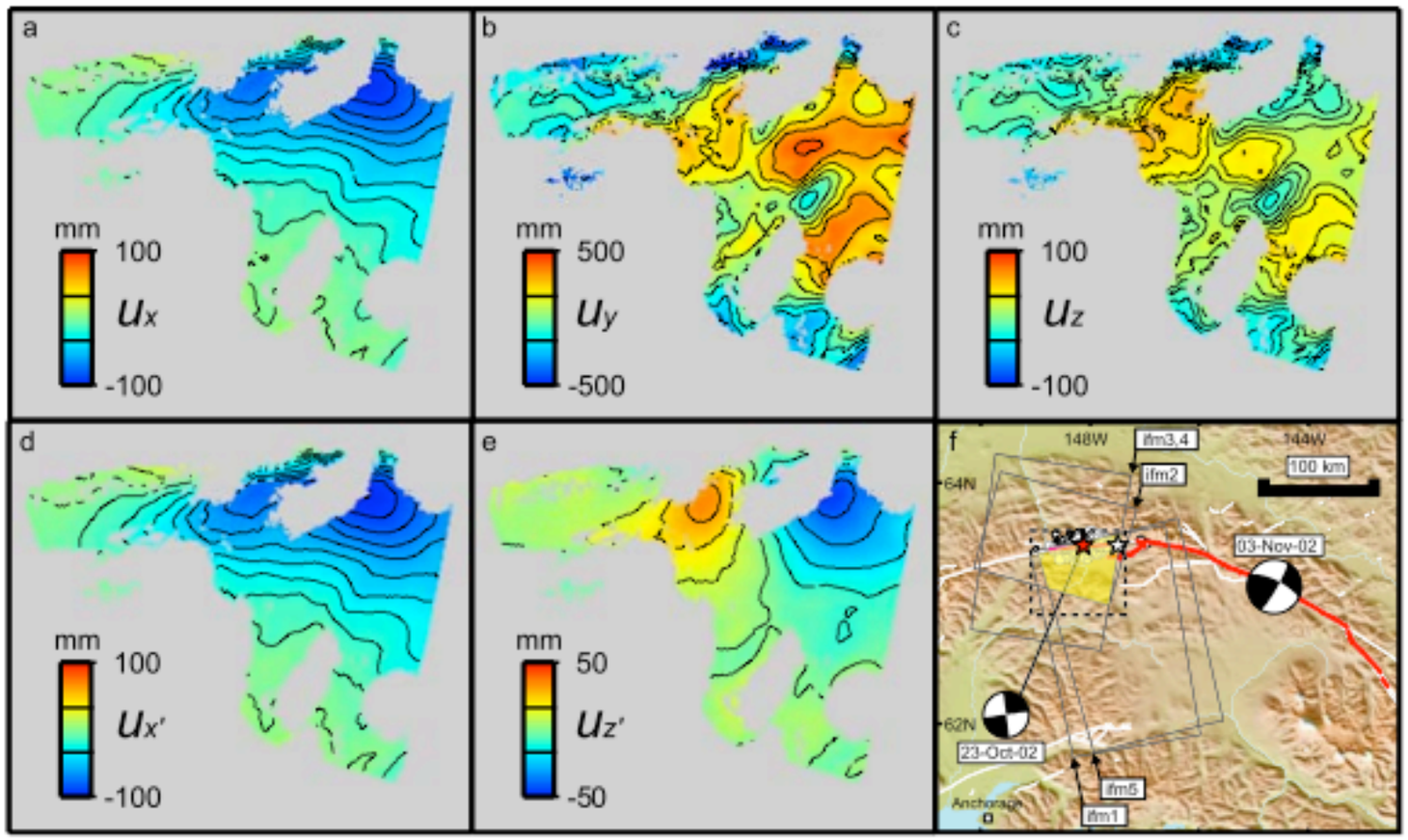

Figure 1. Determining the 3D displacement field for the Nenana Mountain Earthquake. (*a*–*c*) Estimates of u_x, u_y, and u_z respectively. Note that the standard errors in u_x, u_y and u_z are 6, 286 and 41 mm respectively, hence the noisy appearance of u_y and u_z; (*d*, *e*) Solutions for $u_{x'}$ and $u_{z'}$, determined assuming $u_y = 0$. In *a*–*e*, the contour interval is 10 mm, except in *b* where it is 100 mm. The extents of the figure are shown as a dashed box in *f*; (*f*) Location map for the Nenana Mountain earthquake, whose aftershocks are shown in white. Focal Mechanisms for the 23 October and 3 November 2002 earthquakes are from Harvard CMT, and their epicentres are indicated by the stars. Black lines delimit the extents of the InSAR data available for this study, and the region of overlap where 3D displacements were determined is highlighted in yellow. White lines are mapped faults, and the red line is the surface rupture of the 3 November 2002 earthquake.

Wright et al., 2004, GRL